Evidence for formation of DNA repair centers and dose-response nonlinearity in human cells

Teresa Neumaier[a], Joel Swenson[b,c], Christopher Pham[d], Aris Polyzos[d], Alvin T. Lo[d], PoAn Yang[d], Jane Dyball[d], Aroumougame Asaithamby[e], David J. Chen[e], Mina J. Bissell[d,1], Stefan Thalhammer[a], and Sylvain V. Costes[d,1]

[a]Institute of Radiation Protection, Helmholtz Zentrum München, German Research Center for Environmental Health (GmbH), Ingolstädter Landstrasse 1, 85764 Neuherberg, Germany; [e]Division of Molecular Radiation Biology, Department of Radiation Oncology, University of Texas Southwestern Medical Center at Dallas, Dallas, TX 75390; [d]Department of Cancer and DNA Damage Response, Lawrence Berkeley National Laboratory, 1 Cyclotron Road, MS977, Berkeley, CA 94720; [b]Department of Molecular and Cell Biology, University of California, Berkeley, CA 94720; and [c]Department of Genome Dynamics, Lawrence Berkeley National Laboratory, 1 Cyclotron Road, MS977, Berkeley, CA 94720

Contributed by Mina J. Bissell, November 1, 2011 (sent for review September 7, 2011)

The concept of DNA "repair centers" and the meaning of radiation-induced foci (RIF) in human cells have remained controversial. RIFs are characterized by the local recruitment of DNA damage sensing proteins such as p53 binding protein (53BP1). Here, we provide strong evidence for the existence of repair centers. We used live imaging and mathematical fitting of RIF kinetics to show that RIF induction rate increases with increasing radiation dose, whereas the rate at which RIFs disappear decreases. We show that multiple DNA double-strand breaks (DSBs) 1 to 2 μm apart can rapidly cluster into repair centers. Correcting mathematically for the dose dependence of induction/resolution rates, we observe an absolute RIF yield that is surprisingly much smaller at higher doses: 15 RIF/Gy after 2 Gy exposure compared to approximately 64 RIF/Gy after 0.1 Gy. Cumulative RIF counts from time lapse of 53BP1-GFP in human breast cells confirmed these results. The standard model currently in use applies a linear scale, extrapolating cancer risk from high doses to low doses of ionizing radiation. However, our discovery of DSB clustering over such large distances casts considerable doubts on the general assumption that risk to ionizing radiation is proportional to dose, and instead provides a mechanism that could more accurately address risk dose dependency of ionizing radiation.

DNA damage-sensing proteins localize at sites of DNA double-strand breaks (DSBs) within seconds to minutes following ionizing radiation (IR) exposure, resulting in the formation of immunofluorescently stainable nuclear domains referred to as radiation-induced foci (RIF) (1–3). RIF numbers are routinely used to assess the amount of DNA damage and repair kinetics after different treatments (4). However, there is a controversy surrounding the question of whether there is a 1:1 correspondence between RIF and DSBs. For example, pulse field gel electrophoresis (PFGE) analysis suggests that DSBs decay exponentially with time immediately after exposure (5). In contrast, DNA damage-sensing proteins do not instantaneously detect DSBs, leading to delayed kinetics for both detection and resolution. More specifically, the maximum number of 53BP1 or γH2AX RIF is not reached until 15 to 30 min after exposure, and the yield of DSBs predicted by RIF is typically lower than the expected 25–40 DSB/Gy measured by PFGE (4).

Dose response provides another assay for assessing the relationship between DSBs and RIF. Based on theoretical Monte Carlo simulations and PFGE measurements (6, 7), the frequency of DSBs should be highly correlated with radiation dose. Confirming this prediction, two research groups reported that RIF number is proportional to radiation dosage from 1 mGy to 2 Gy (8, 9). In both studies, methods were applied to identify "real" RIF at low doses, where frequencies may be close to background levels before IR (e.g., 10 mGy would lead to about 0.3 DSB/cell). They either used cells with very low γH2AX background foci (i.e., 0.05 background foci/cell in primary human lung MRC-5 fibroblasts) (8), or performed live studies with a tagged DNA damage marker (i.e., 53BP1-GFP) and disregarded foci that were present before exposure to IR (9). However, there were discrepancies between these two studies. One study reported a 1:1 correspondence between RIF and DSBs, with a maximum of 35 γH2AX RIF/Gy at 3 min post-IR exposure (8), whereas the other study reported RIF frequencies were maximal much later (i.e., 30 to 60 min post-IR), with different proportionality; i.e., 16–20 53BP1-GFP RIF/Gy for human HT1080 and 60 53BP1-GFP RIF/Gy for immortalized human bronchial epithelial cells (9). These discrepancies cast some doubts on the one-to-one correspondence between RIF and DSB and also show that cell type and methods of analysis both play a crucial role in RIF quantification. Furthermore, dose/response linearity is not always observed. For example, in normal human fibroblasts (1) and in hamster V79 cells (10), we observed a maximum of 18–24 γH2AX RIF/Gy after exposure to less than 1 Gy of X-rays, compared to 13–15 γH2AX RIF/Gy for 1–4 Gy. Similarly, human fibroblasts showed a slight decrease with averages ranging from 21 to 17 RIF/Gy between 0.05 and 0.25 Gy, which was consistent across 18 independent lines (11).

Most studies measure RIF only at discrete times after the induction of damage. This means that the temporal complexity of the biochemical response, primarily initiated by DNA damage, is often neglected. However, temporal delays in RIF formation relative to DSBs as well as different resolution times for RIF complicate the interpretation of RIF numbers. In addition, even when kinetic studies are performed, the number of RIF reported at any given time after IR can never reflect the total number of RIF that have been produced by IR, as all RIF that have already been resolved or that have not yet been produced are not counted.

Here, we present a mathematical formalism that extracts the absolute number of RIF from RIF kinetics data. By integrating this biophysical model with a standardized high-content imaging methodology (2), we demonstrate the ability to get reproducible RIF results from different research laboratories. Miniaturization of cell cultures, using microwell slide technology, were also applied to further accelerate and normalize sample treatment and processing. This comprehensive quantitative analysis challenges the concept of linearity between IR dose and RIF yield and suggest the existence of DNA repair center in human cells.

Author contributions: M.J.B. and S.V.C. designed research; T.N., J.S., C.P., A.P., A.T.L., P.Y., J.D., and S.V.C. performed research; J.S., A.A., D.J.C., M.J.B., S.T., and S.V.C. contributed new reagents/analytic tools; T.N., C.P., and S.V.C. analyzed data; and M.J.B. and S.V.C. wrote the paper.

The authors declare no conflict of interest.

Freely available online through the PNAS open access option.

See Commentary on page 351.

[1]To whom correspondence may be addressed. E-mail: svcostes@lbl.gov or mjbissell@lbl.gov.

This article contains supporting information online at www.pnas.org/lookup/suppl/doi:10.1073/pnas.1117849108/-/DCSupplemental.

Results

Validation of RIF Yield and Formation-Disappearance Kinetics Models Using Live Cells Exposed to X-Rays. We propose a mathematical model to fit the kinetics of RIF formation, which can deduce the absolute number of RIF produced by a given dose of IR from the net number of RIF measured at any time point (see *Materials and Methods*). Live cell imaging is ideal to validate such a model, because it simultaneously measures the number of RIF at any given time and the number of RIF accumulated since the time of exposure to X-rays. To test the validity of our model, we fitted with Eq. **1** the number of RIF measured in MCF10A transiently transfected with 53BP1-GFP. Both the number of RIF counted at each time frame, as well as the cumulative number of RIF counted after IR exposure, were scored (representative snapshots and kinetics are shown in Figs. 1*A* and 2*A* for 0.1 and 1 Gy, respectively). If Eqs. **1** and **2** were correct, the cumulative RIF counts (red curves shown in Figs. 1*B* and 2*B*) should converge over time to a constant value equal to the total number of RIF/Gy (α).

Confirming this biophysical model, fits of the net kinetics (green curves in Figs. 1*B* and 2*B*) with Eq. **1** led to an α value that matched the total cumulated yield. In addition, live cell imaging revealed that the total number of RIF produced by IR was not proportional to dose, and was relatively lower at higher doses (73 RIF/Gy vs 28 RIF/Gy at 0.1 and 1 Gy, respectively). In addition, RIF induced by low doses appeared more slowly and were resolved faster than after 1 Gy, as indicated by the reported formation and resolution half-lives on the graph ($T_{1/2}$). Three-dimensional time lapse using confocal microscopy on human fibrosarcoma HT1080 stably transfected with 53BP1-GFP showed very similar properties for 0.05, 0.1, and 1 Gy (Fig. S1). Finally, monitoring the intensity profiles of individual RIF during time lapse imaging identified changes in RIF size and intensity during focus formation (blue dashed rectangle in Figs. 1*A* and 2*A*). The relative intensity profiles for individual foci (1D intensity cross-section of focus location normalized to the average 53BP1 intensity outside foci regions) and their averages are shown in Figs. 1*C* and 2*C*. Even though no difference in size could be observed, with an average RIF diameter of 0.64 μm for both high and low dose, a threefold increase of RIF intensity was measured after high dose.

High-Content Analysis on Fixed Specimens Confirm Nonlinear RIF Yield with Dose. In order to quantify a larger dataset representing endogenous levels of proteins, we analyzed arrays of fixed MCF10A by immunostaining for 53BP1. As described in *Materials and Methods*, detection of RIF was done automatically, using improved in-house RIF detection algorithms (2). The computer scoring obtained in this manner was corroborated for a subset of cells counted manually at 30 min after different doses of X-ray (from 0.05 to 2 Gy; Fig. S2). Fig. 3 *A–C* show representative images for selected doses, showing the efficiency of the algorithm for separating touching foci. Applying this approach for fitting average counts of seven independent experiments measured at various doses of X-rays collected over a 24-h time course, we observed excellent agreement with Eq. **1** (Fig. 3*D*). All fitted coefficients for Eq. **1** are summarized in Table 1. Similarly to what we observed with 3D time lapse, the absolute number of 53BP1 RIF normalized to dose (α in RIF/Gy per nucleus) decreased approximately 4-fold between 0.1 and 2 Gy (approximately 64 ± 6 to 16 ± 2 RIF/Gy, after 0.1 and 2 Gy, respectively). This decreasing trend was statistically significant (P value < 0.01 using t test). RIF kinetics were also dose dependent: RIF formation was twice as fast and RIF resolution was approximately 5 times slower at 2 Gy versus 0.1 Gy (see Table 1). Both k_1 and k_2 dose dependence were significant (P value < 0.05 using one-way ANOVA). To test if the dose-dependent DNA damage response was specific to breast epithelial cells, the same measurements were made on immortalized human skin fibroblasts (HCA2) grown as confluent populations (1), where we observed a similar trend, with a 1.7-fold decrease of RIF yield α, a 2.5-fold increase in 53BP1 RIF induction rate, and a 20-fold decrease in RIF resolution rate between 0.1 and 2 Gy (Fig. S3).

To test the validity of the mathematical model further, we perturbed the rates of RIF formation or RIF removal by inhibiting ataxia telangiectasia mutated (ATM) kinase activity with KU55933 (see *Materials and Methods*). ATM inhibition was confirmed by measuring the reduction of phosphorylated p53 at S15 (Fig. 3*E*). As expected, the overall number of RIF was largely diminished (Fig. 3*F*). However, the same behavior was observed; i.e., RIF yield dropped by 2-fold between 0.1 and 2 Gy (25 ± 17 vs. 12 ± 2 RIF/Gy). Fitted parameters are shown in Fig. 4 *A–C*. Interestingly, detection half-lives were comparable with or without ATM inhibition across all doses, whereas resolution was significantly slower at high doses when ATM was inhibited (significant difference between 15.4 ± 1.8 h with inhibition and 5.7 ± 1.6 h without inhibition, after 2 Gy). This indicates that DSBs

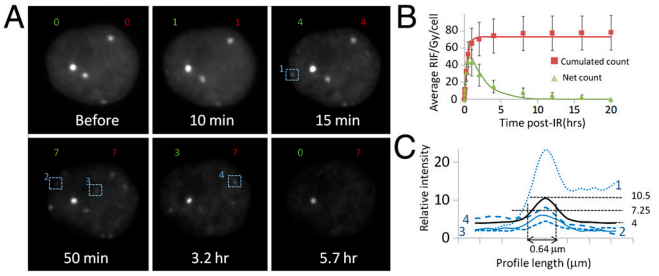

Fig. 1. Time-lapse imaging of MCF10A transiently transfected with 53BP1-GFP after exposure to 0.1 Gy of X-rays. (*A*) Representative snapshots of best focal plane for a 3D time lapse. Counting was done manually in two different ways: (*i*) static measurement, indicating the number of RIF/cell at the time it is measured (green numbers and graphs); (*ii*) cumulated measurement, indicating at any time the overall number of different RIF that have appeared since time 0 (red numbers and graphs). The 53BP1 nuclear bodies visible before IR were not included in RIF counts. (*B*) RIF counts from 40 different time lapses (three independent experiments) leads to an average for $T_{1/2_{induction}} = 15$ min, $T_{1/2_{resolution}} = 1.4$ h, $\alpha = 73$ RIF/Gy. Fits are shown as solid lines, and experimental points as red square for cumulated counts and green triangles for net counts ($R^2 = 0.98$ and t test P value = 0.005 for the fit). (*C*) One-dimensional intensity profiles of four different regions of interest indicated by blue dash box in *A*. The average profile is indicated by solid curve and used to evaluate the average size of a focus (defined as the full width at half maximum of the peak).

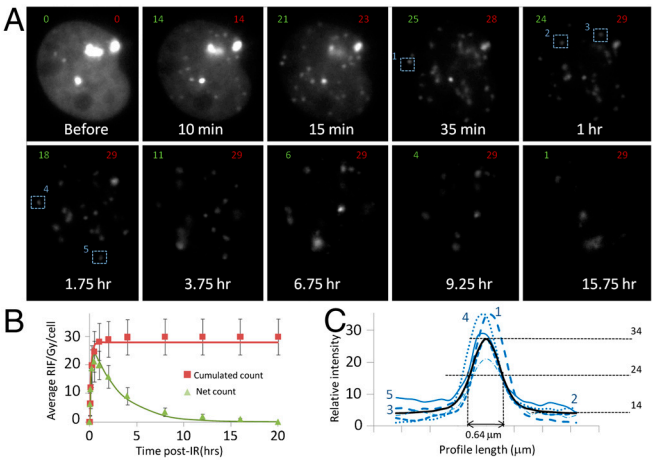

Fig. 2. Time-lapse imaging of MCF10A transiently transfected with 53BP1-GFP after exposure to 1 Gy of X-rays. (*A*) representative snapshots of best focal plane for a 3D time lapse. (*B*) RIF counts from 21 different time lapses (three independent experiments) leads to an average for $T_{1/2_{induction}} = 6.5$ min, $T_{1/2_{resolution}} = 2.1$ h, $\alpha = 28$ RIF/Gy. $R^2 = 0.99$ and t test P value = 0.003 for the fit. (*C*) One-dimensional intensity profiles of five different regions of interest indicated by blue dash box in *A*.

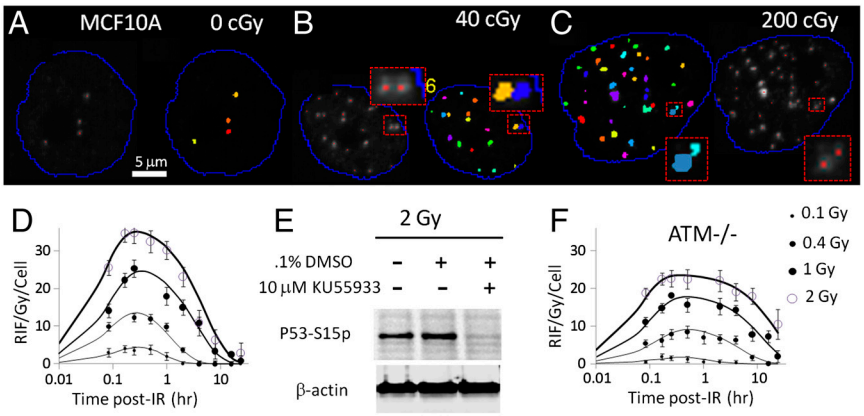

Fig. 3. Representative time response of background corrected RIF per nucleus in MCF10A exposed to various doses of X-rays and immunostained for 53BP1. (*A*, *B*, and *C*) Maximum intensity projections of representative 3D stack images at various doses (red dots indicate detected 53BP1 RIF) are accompanied with the same nucleus overlaid with the full shape identification of an RIF and the ability of the algorithm to separate touching RIF even at the maximum dose (*C*—2 Gy, see enlargement). In these images, each RIF is labeled by the algorithm with a different color to facilitate individual visualization. (*D*) Time response under normal media conditions for one experiment out of seven performed (average R^2 across all doses is 0.98 and *t* test *P* value is less than 0.01). Experimental data points (circles) get larger with dose (0.1, 0.4, 1, and 2 Gy, respectively), and they correspond to averages for approximately 1,000 nuclei per point, with their corresponding standard deviations. Solid lines are least-square fits using Eq. **1** for each time response. (*E*) Inhibition of ATM measured by Western blot of P53-S15p. (*F*) Time response under ATM inhibition (average R^2 across all doses is 0.99 and *t* test *P* value is less than 0.01), based on one experiment.

requiring longer repair time are still being detected at the same rate, in the absence of ATM kinase activity.

RIF Analysis in Human Cells Exposed to Dense IR Reveals Self-Exclusion of Nearby RIF. In order to further explore the saturation effect of RIF numbers observed at higher dose, one would need to look at the DNA damage response for doses of X-rays higher than 2 Gy. However, at such high doses there are several confounding factors: (*i*) there is the difficulty of resolving high numbers of RIF in the nucleus, and (*ii*) the physiological effects on the cells manifest at higher doses (e.g., toxicity, cell cycle arrest, etc.). In order to circumvent these issues, we used high-energy Fe ions (1 GeV/atomic mass unit), referred to as HZE (High *Z* and energy). As illustrated in Fig. S4, HZE particles typically deposit part of their energy along linear tracks referred to as cores, and the other part is deposited from electrons randomly outside the core (i.e., delta rays). The radius of the core is about 10 nm for 1 GeV/atomic mass unit Fe ions, whereas delta rays radiate approximately 270 μm from the track (12, 13). As we described previously (2), we have developed imaging tools that automatically identify these tracks and can discriminate RIF along the tracks from random RIF in the nucleus (presumably generated by delta rays; Fig. S4). In order to account for RIF and physiological chromatin movement over time, all RIF detected within a 0.5-μm radial distance from the particle trajectory were considered "core RIF." Assuming a radial dose distribution decreasing as the distance square from the core (14, 15), we estimated a dose of 26 Gy within the 0.5-μm radius track, and 0.17 Gy from delta rays dispersed outside that region (Fig. S4). Thus, HZE particle radiation allowed us to compare two compartmentally distinct radiation doses within the same cell (representative images shown in Fig. 4 *A* and *B*). We noted that core RIF sizes and intensities (Fig. 4*C*) were comparable to 1-Gy X-ray foci (Fig. 2*C*) as early as 1.5 min post-IR. However, core RIF were larger and brighter by 30 min post-IR. In contrast, delta-ray RIF size and intensity kinetic was comparable to X-rays (Fig. 4*C* vs Fig. 1*C*, respectively).

In addition, our results confirmed what was observed for X-rays; i.e., high local doses along the track led to much faster RIF induction (approximately 5-s half-lives) and slower RIF resolution (approximately 10-h half-lives) than in the low-dose region of the delta rays (2.8 min and 3.3 h, respectively). The fitted coefficients are plotted against all other conditions studied in this work in Fig. 5 *A*–*C* and listed in Table 1. Note that the measured RIF yield along the tracks was fitted to be 0.83 RIF/μm but could not be plotted against other α values in Fig. 5*A* because it was in a different unit.

Similar differences in RIF kinetics between track RIF and delta-ray RIF were also observed in live cell imaging of MCF10A cells transiently transfected with 53BP1-GFP (Fig. S5). Time-lapse imaging showed that after initial foci formation there were few new foci appearing along the tracks, whereas new delta-ray RIF outside the track kept appearing during the initial 30-min post-IR period. Similar results were observed also in stably transfected human bronchial epithelial cells exposed to 1 GeV/atomic mass unit O ions (Fig. S6).

Discussion

Single time or single dose measurements are snapshots and might not capture the complexity of the IR response of DNA damage-sensing proteins. Here, we present a methodology and a mathematical kinetic model that can characterize the DNA damage response simultaneously across both time and dose levels. Our results provide a more accurate model of RIF dose response, and underscore fundamental concerns about static image data analysis in the dynamic environment of the living cell. We observe that as the number of DSB increases in a cell, the number of RIF does not increase proportionally and the kinetics of RIF formation/disappearance is altered; RIF appear faster but remain longer

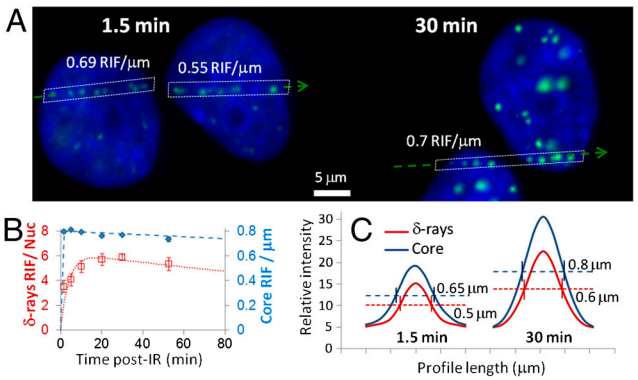

Fig. 4. Representative time response of background corrected RIF per nucleus in MCF10A exposed to 1 GeV/atomicmass unit Fe ions and immunostained for 53BP1. (*A*) Representative images for 1.5 and 30 min post-IR, illustrating which RIF are classified "core RIF" vs "delta-ray RIF". (*B*) Time response averaged over five independent experiments cumulating more than 1,000 tracks per time point and experiment. Delta-ray RIF are reported as RIF/nucleus per Gy (red), where as core RIF are reported as RIF/μm (blue). (*C*) Average normalized intensity profiles at 1.5 and 30 min post-IR for core and deltay-ray RIF ($N = 20$ for each profile—RIF diameters are shown as the full width at half maximum of the peaks).

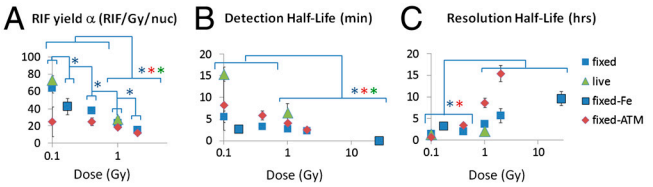

Fig. 5. Average fitted parameters for all time responses measured in human MCF10A. Four conditions are considered (fixed, normal condition, immunostaining of 53BP1, $N = 7$; fixed-ATM, ATM inihibition and immunostaining of 53BP1, $N = 1$; fixed-Fe, 53BP1 immunostaining after exposure to 1 GeV/atomic mass unit Fe, with estimated doses along ion tracks of 26 Gy and outside tracks of 0.17 Gy, $N = 5$; live, time-lapse imaging of MCF10A transiently transfected with 53BP1-GFP after exposure to 0.1 and 1 Gy of X-rays, $N = 3$). All trends are statistically significant with respect to dose using one-way ANOVA test ($P < 0.01$ for α and $P < 0.05$ for k_1 and k_2). Statistical differences between dose points are tested with the Tukey–Kramer test and are indicated by an asterisk with the color corresponding to the group when significant. (*A*) Absolute RIF yield α (RIF/Gy per nucleus), showing a decrease with dose. (*B*) RIF induction half-life ($\ln(2)/k_1$), showing a faster induction with dose. (*C*) RIF disappearance-resolution half-life ($\ln(2)/k_2$) showing a slower RIF resolution with dose.

in the cells as dose levels increase. These nonlinear processes cast considerable doubts on the general assumption that risk to IR is proportional to dose and could be interpreted as the consequence of DNA repair centers in human cells.

Clustering of DSB into Repair Centers at High Dose. As recently reviewed (4), most studies in the literature report RIF yield well below the expected 25–40 DSB/Gy measured by PFGE in cells in the G1 part of the cell cycle (5, 8). This probably reflects the fact that what is measured at any time point is the net number of RIF that have formed since radiation, which does not account for RIF that have already been resolved, or for RIF that have not yet appeared. The time-lapse imaging presented here shows clearly that RIF formation continues to occur well beyond initial IR exposure time. In addition, our biophysical model fits well the kinetics curves observed for the number of RIF per nucleus and accounts for these missing RIF. These fits suggest that the absolute RIF yield normalized to dose (α) is not constant but drops 4-fold between 0.1 and 2 Gy. The lower yield of α at high dose cannot be explained by depletion of the pool of 53BP1. Indeed, protein depletion would only lead to dimmer foci, not fewer foci. Furthermore, RIF number saturation cannot be due to overlapping foci because the expected spatial random distribution of DSBs simulated by computer (see *Materials and Methods*) predicts average distances easily resolvable by light microscopy at the highest dose considered (2 Gy). Similarly, using radiation that deposits a high amount of energy along a tightly defined track, we observe approximately 0.7–0.8 RIF/μm along 1 GeV/atomic mass unit Fe (linear energy transfer, LET = 150 keV/μm), contrary to a theoretical value based on physical considerations of approximately 1.1 DSB/μm (2). In addition, when cells are exposed to ions with a hundred times higher energy densities (e.g., uranium ions with LET of 14,300 keV/μm and expected approximately 100 DSB/μm), RIF frequencies remain in the same order of magnitude (i.e., 0.96 XRCC1 RIF/μm) (16), suggesting full saturation of the number of RIF. One potential explanation for this apparent saturation is the existence of repair centers with a minimum interdistance of approximately 1 μm. If repair centers exist, as the local dose increases, the probability of having two DSBs migrating into one common RIF increases, leading to lower RIF counts per dose, faster induction, and slower resolution.

Table 1. Fitted parameters for various doses of X-rays, and for delta rays and track core time response to 1 Gy of 1 GeV/atomic mass unit Fe

	Average			Standard error		
Dose (Gy)	α, RIF/Gy	T1/2_1, min	T1/2_2, h	α, RIF/Gy	T1/2_1, min	T1/2_2, h
Controls MCF10A ($N = 7$)						
0.1	64	5.6	1.4	6	1.3	0.5
0.4	38	3.4	2.0	2	0.4	0.6
1	23	2.8	3.8	3	0.5	0.6
2	15	2.4	5.7	2	0.1	1.6
ATM inhibition MCF10A (one experiment)						
0.1	25	8.3	0.7	17	5.8	0.5
0.4	25	5.9	3.5	4	1.1	0.6
1	19	4.2	8.7	2	0.5	1.1
2	12	2.6	15.4	2	0.3	1.9
Live 53BP1-GFP in MCF10A ($N = 3$, 5 to 10 cells per experiment)						
0.1	73	15.4	1.4	5	1.6	0.2
1	28	6.5	2.1	3	2.1	0.1
1 GeV/atomic mass unit Fe in MCF10A ($N = 5$)						
0.17 (delta rays)*	43	2.8	3.3	9	0.2	0.8
27 (core)*	—	0.1	9.6	—	0.01	1.6

*Dose estimation, based on microdosimetry computations of 1 GeV/atomic mass unit Fe exposure (Fig. S7)

Note that a distance of 1–2 μm is in good agreement with previous estimate of the distance between two separate DSBs which can explain DSB misrejoining data leading to the classic supralinear dose dependence observed for radiation-induced chromosomal rearrangements (17, 18). Time-lapse imaging also suggests that if DSB clustering takes place, it happens before an RIF is formed, because RIF clustering was not observed within the first 30 min post-IR. On the other hand, we did observe the merging of RIF over hours post-IR. RIF merging over long time course has already been described along high energy density tracks (19), and has been interpreted as transient clusters that eventually separate again (20).

In this work, we hypothesize that DSB clustering occurs rapidly after IR and that RIF formation reflects the repair machinery put in place around one cluster of DSBs. DSB clustering can then be rewritten as follows: $\beta \times \mathrm{DSB} \xrightarrow{k_1} \mathrm{RIF} \xrightarrow{k_2} \mathrm{RIF}_{\mathrm{resolved}}$, where $\beta(D)$ is the average number of DSB within one RIF. Assuming 35 DSB/Gy, $\beta = 35/\alpha$ and based on our data, it increases with dose: $\beta \sim 1$ DSB/RIF at 0.4 Gy, suggesting a one-to-one correspondence, whereas there would be $\beta \sim 2.3$ DSB/RIF after 2 Gy. Resolving these equations would then show that the real induction rate for RIF is in fact $k'_1 = \beta.k_1$, where k_1 is dose independent and only reflects the time it takes to detect one DSB. The increasing induction rate with doses would then simply reflect β increasing with dose. Our data also show that RIF intensity is larger for higher doses while RIF sizes are similar. This suggests the existence of a well defined chromatin scaffold for these repair centers, with the presence of multiple DSB requiring more 53BP1 proteins compacted within the same structure. Note, however, that the rigidity of these repair centers is not absolute; this is because we noticed that RIF are both brighter and larger for extremely high doses along HZE tracks.

DNA damage repair centers have been clearly established in *Saccharomyces cerevisiae* (21), but they remain hypothetical in mammalian cells, as initially suggested by Savage (22, 23). However, there are some data suggesting their existence in human cells. For example, there were indications in human blood cells that chromosomal rearrangements observed after exposure to high LET could be explained by localized movement of chromatin containing damaged DNA into local repair centers (24). Following up on this work, it was more recently shown that increasing LET of an α particle did not increase the total number of aberrations per track traversal, and instead increased the ratio of complex to total aberrations (25). Therefore, if DSB clustering occur, as LET goes up (for LET > 100 keV/μm), RIF linear frequencies would not change significantly but each RIF would be made of more DSBs, increasing the probability of complex chromosomal rearrangements. In agreement with this theoretical argument, high-resolution imaging of high-LET tracks in combination with Monte Carlo simulation have suggested recently the

presence of multiple DSBs within one single RIF (26). Similarly, a recent theoretical follow-up study taking into account the track structure of high-energy ions and the supercoiled topography of DNA confirmed that multiple DSB can be contained within one single RIF (27). Finally, we previously showed that spatial RIF distribution along high-LET tracks implied relocalization of DSBs rapidly post-IR (2), and an independent study reached the same conclusion as 53BP1 RIF pattern along tracks differed significantly from theoretical expectations assuming a simple model of homogenous chromatin distribution (28). Whereas our data bring additional evidence of the existence of repair centers in human cells, the mechanisms by which such clustering take place remain entirely unknown at this point: Are DSB clusters the result of random coalescence induced by DNA damage binding complexes (19) or is there an active transport of DSB toward preexisting repair centers?

RIF Resolution Kinetics Reflect both Break Complexity and Break Density. If we were to accept the classic definition that a complex DSB is made by at least three single-strand breaks within 10 base pairs (29), then it is estimated that 20 to 30% of DSBs are complex after exposure to low-LET radiations. In contrast, 70% of the damage induced by the ion used in this work is complex (30). The resolution kinetics constants reported here show large difference of resolution kinetics between these two radiation qualities, with half-lives for RIF resolution as fast as 1.4 h after 0.1 Gy of X-rays and as slow as 10 h after high-LET for an estimated local dose of 26 Gy along Fe ions tracks. In comparison, using PFGE after higher doses of X-ray (>10 Gy), the fast repair half-life associated with simple DSB is approximately 5–30 min and the slow repair half-life is approximately 4–10 h (31, 32). Therefore, even though RIF resolution does not only reflect DSB repair, but delays due to the clearing of 53BP1 after repair (33, 34), IR-induced DSB repair kinetics correlate well with RIF disappearance. Classically, the different DSB repair kinetics between different LET has been interpreted as additional delays for repairing complex DSBs. However, our work suggests that using the same LET, local dose effects alone can affect resolution kinetics: There is a 4-fold increase in RIF resolution half-lives between 0.1 and 2 Gy of X-rays (5.7 h at 2 Gy). Therefore, we conclude that slower DSB repair kinetics may not only reflect the presence of complex breaks, but also the presence of multiple DSB within one repair center, leading to a repair machinery having difficulty handling multiple ends of DNA strands in the same location.

High RIF Yield at Low Dose for MCF10A. Under normal conditions, we detect many more RIF than expected in MCF10A after 0.1 Gy (64 RIF/Gy detected vs 35 RIF/Gy expected), especially in live cell imaging (73 RIF/Gy). Note that this leads to β value less than 1. This effect seems to be cell dependent: similar but more modest yields were observed for live imaging of fibrosarcoma cells HT1080 with 49 RIF/Gy and 40 RIF/Gy following 0.05 and 0.1 Gy, respectively; and 30 RIF/Gy following 0.1 Gy in fixed normal human skin HCA2. In addition, we have not confirmed that the increase of RIF yield at low dose correlates with other surrogate markers of DNA damage such as chromosomal aberrations or micronuclei.

We also show here that ATM inhibition result in 3-fold reduction of α after 0.1 Gy of X-rays with a yield of 25 RIF/Gy, whereas no significant reduction of α is observed after 2 Gy with a yield of 12 RIF/Gy comparable to 15 RIF/Gy under normal conditions. This suggests that the higher RIF yield at low-dose IR is ATM dependent. Because IR can induce heterochromatin decondensation in *Drosophila* cells (35) or in mammalian cells (36), one could thus hypothesize that low doses of IR induce a global but subtle chromatin reorganization, which could lead to increase foci that may not necessarily relate to more DNA damage. In agreement with this hypothesis, ATM has been shown to autophosphorylate and consequently phosphorylate H2AX when nuclear volumes are dilated by using hypotonic media (37). Similarly, it has been shown that hypotonic conditions alone are sufficient to induce binding of 53BP1 to chromatin (38).

Impact of Results for Regulating Risk of IR on Human Populations. The current literature has assumed the linear-no-threshold hypothesis (LNT), which implies that any amounts of IR are harmful. LNT is used to set dose limits for radiation occupational workers or the general public. The LNT is based mainly on data from the Japanese atomic bomb survivors and secondarily on arguments involving the dose-response of surrogate endpoints. Gene mutations are thought to be the initiating events of cancer and they can occur via misrejoining of two DNA DSBs or via point mutation. Physical laws lead us to believe DSB frequencies are proportional to dose. Therefore, it is well accepted that point mutations are linear with dose because it requires only one DSB, whereas DSB misrejoinings are dependent to the dose squared (39). In the dose range of radiation cancer epidemiology, the quadratic term is almost always negligible, especially at low dose rates, as the first lesion is probably repaired before the second mutation occurs (40). However, the amount of DSB clustering at 1 Gy suggests a much higher quadratic term for DSB misrejoining than expected. Therefore, extrapolating risk linearly from high dose as done with the LNT could lead to overestimation of cancer risk at low doses.

Materials and Methods

Cell Culture. Nonmalignant human mammary epithelial cells (MCF10A, purchased from ATCC) were grown on 8-well Lab-Tek chambered coverglass (Nalge Nunc International) or on 48-spot functionalized glass slides (AmpliGrid, Beckman Coulter GmbH). The cells were grown until they formed a monolayer (approximately 85% confluent) prior to irradiation. See *SI Materials and Methods* and Fig. S7 for full details.

Irradiation and ATM Inhibition. The cells were fixed for immunofluorescence at specific intervals after exposure to X-rays. We typically refer to "low dose" or "high dose" as doses below or equal to 0.1 Gy or larger than 1 Gy, respectively. For high-LET IR, cells were irradiated at the accelerator beam line of the National Aeronautics and Space Administration Space Research Laboratory at Brookhaven National Laboratory. ATM activity was inhibited by incubating cells with 10 μM of ATM specific inhibitor KU55933 (Calbiochem) from 1 h pre-IR until cells were fixed, as previously described (41).

Immunostaining and Imaging. We are only briefly describing these procedures. For complete information, see *SI Materials and Methods*. Immunostaining using anti-53BP1 (rabbit polyclonal, Bethyl Laboratories A300-272A) was performed according to previous staining protocol (1). For image acquisition, both live and fixed MCF10A were imaged using a Zeiss plan-apochromat 40X dry objective (N.A. of 0.95) at a fixed exposure time. Nondeconvolved 3D stacks were acquired and used for image analysis (10 slices of 0.5-μm steps for fixed cells and 3 slices of 1-μm step for live cells). All image manipulations, foci analysis, and statistics were done with Matlab (MathWorks, Inc.) and DIPimage (image processing toolbox for Matlab, Delft University of Technology). In contrast to previous intensity-based methods for RIF identification (42), we used a pattern recognition approach to detect RIF by applying a wavelet morphological filter to enhance RIF peaks in the image while reducing noise from nonspecific signals (43). Nuclear space occupied by RIF was identified by applying a constant threshold on the wavelet filtered image, and watershed algorithm was used to separate touching RIF. To test if focus size could affect the accuracy of automatic RIF detection, we applied the software on simulated data where foci sizes and densities had different values (i.e., 1 to 40 foci/nucleus were simulated with four distinct sizes: 0.1, 0.4, 1.3, and 2.4 μm^3; Fig. S8). We concluded that foci overlap at the highest foci density (40 foci/nucleus) would be negligible in real data and therefore would not impact RIF counts. Finally, in order to extract the number of "real" RIF from the number of background foci in each scored nucleus, we introduced a background subtraction method that assumes the measured RIF distribution is the result of a convolution between the "real" RIF distribution and the background foci distribution (Fig. S9). For quantification of RIF in live cells, we counted both the cumulative and instantaneous number of RIF manually in 3D time-lapse images. Time interval varied between experiments and

was generally set to 10-min interval for the first hour, followed by 30-min interval afterwards. This setting was optimum to minimize phototoxicity and specimen bleaching. Because of the difficulty of software to track individual foci in successive time lapse, analysis had to be done manually in a blind manner on processed images.

Mathematical Model of DSB Detection and RIF Formation. In order to interpret RIF kinetics in an unbiased manner, we introduce a simple mathematical model describing RIF formation where one DSB is detected at a rate k_1 leading to one RIF, and one RIF is resolved after repair at a rate k_2, assuming both processes are irreversible. This model can be noted as followed: $\mathrm{DSB}\xrightarrow{k_1}\mathrm{RIF}\xrightarrow{k_2}\mathrm{RIF}_{\mathrm{resolved}}$. Let C_0 and C_1 be the average number of DSB and RIF per nucleus at time t, respectively. This kinetic model translates then into the following set of differential equations:

$$\begin{cases} \frac{dC_0}{dt} = -k_1 C_0 \\ \frac{dC_1}{dt} = k_1 C_0 - k_2 C_1 \end{cases} \underset{\Rightarrow}{C_1(0)=0} \begin{cases} C_0(t) = \alpha D.e^{-k_1 t} \\ C_1(t) = \frac{\alpha D k_1}{k_2 - k_1}\left(e^{-k_1 t} - e^{-k_2 t}\right) \end{cases} \quad [1]$$

where α is the number of naked DSB/Gy before formation of RIF and D is the dose delivered to the cell. α should be constant for all doses. Further details are provided in *SI Materials and Methods* regarding the way Eq. **1** is fitted. Note that one could modify the kinetic model presented here to separate rapid repair of simple lesions and slow repair of complex lesions as it has been previously suggested from PFGE DSB kinetics (31, 32). This would, however, lead to an additional kinetic constant, which would result in multiple solutions for the same fit. We therefore opted for a mathematical model that can be resolved with less ambiguity, using only one rate for induction and one rate for resolution.

$C_1(t)$ in Eq. **1** can be used to fit the number of RIF at a given time (static measure). However, one can also measure using time-lapse imaging the total number of RIF that have been produced since $t = 0$ (cumulated measure). This can be described mathematically as

$$C_c(t) = \alpha D(1 - e^{-k_1 t}). \quad [2]$$

Eq. **2** is derived simply by setting $k_2 = 0$ and using the same formalism as in Eq. **1**.

Note that the corresponding half-life for k_1 and k_2 (i.e., $t_{1/2_k} = \ln(2)/k$) are reported in the text. $t_{1/2_{k1}}$ represents the time it takes for half of all DSBs to be detected as RIF. $t_{1/2_{k2}}$ represents the time it takes for half of the total number of RIF to be resolved.

ACKNOWLEDGMENTS. We thank M.H. Barcellos-Hoff from New York University School of Medicine for providing earlier leadership and support and R. Sachs from University of California, Berkeley, Math Department, J. Pluth, I. Chiolo, J. Mott, D. Ciobanu, and G. Karpen from Lawrence Berkeley National Laboratory for their constructive comments on the manuscript. S.V.C. is supported by National Aeronautics and Space Administration Specialized Center for Research in Radiation Health Effects (NNJ09HC64I) and the Low Dose Scientific Focus Area, US Department of Energy (DE-AC02-05CH11231). M.J.B. is supported by the US Department of Energy, Department of Defense, and the National Institutes of Health. T.N. and S.T. were supported by the Excellence Cluster "Nanosystems Initiative Munich." A.A. and D.J.C. were supported by National Aeronautics and Space Administration (NNZ07AU42G).

1. Costes SV, et al. (2006) Imaging features that discriminate between foci induced by high- and low-LET radiation in human fibroblasts. *Radiat Res* 165:505–515.
2. Costes SV, et al. (2007) Image-based modeling reveals dynamic redistribution of DNA damage into nuclear sub-domains. *PLoS Comput Biol* 3:e155.
3. Rogakou EP, Pilch DR, Orr AH, Ivanova VS, Bonner WM (1998) DNA double-stranded breaks induce histone H2AX phosphorylation on serine 139. *J Biol Chem* 273:5858–5868.
4. Costes SV, Chiolo I, Pluth JM, Barcellos-Hoff MH, Jakob B (2010) Spatiotemporal characterization of ionizing radiation induced DNA damage foci and their relation to chromatin organization. *Mutat Res* 704:78–87.
5. Stenerlow B, Karlsson KH, Cooper B, Rydberg B (2003) Measurement of prompt DNA double-strand breaks in mammalian cells without including heat-labile sites: Results for cells deficient in nonhomologous end joining. *Radiat Res* 159:502–510.
6. Goodhead DT, Nikjoo H (1989) Track structure analysis of ultrasoft X-rays compared to high- and low-LET radiations. *Int J Radiat Biol* 55:513–529.
7. Erixon K, Cedervall B (1995) Linear induction of DNA double-strand breakage with X-ray dose, as determined from DNA fragment size distribution. *Radiat Res* 142:153–162.
8. Rothkamm K, Lobrich M (2003) Evidence for a lack of DNA double-strand break repair in human cells exposed to very low X-ray doses. *Proc Natl Acad Sci USA* 100:5057–5062.
9. Asaithamby A, Chen DJ (2009) Cellular responses to DNA double-strand breaks after low-dose gamma-irradiation. *Nucleic Acids Res* 37:3912–3923.
10. MacPhail SH, et al. (2003) Expression of phosphorylated histone H2AX in cultured cell lines following exposure to X-rays. *Int J Radiat Biol* 79:351–358.
11. Wilson PF, et al. (2010) Inter-individual variation in DNA double-strand break repair in human fibroblasts before and after exposure to low doses of ionizing radiation. *Mutat Res* 683:91–97.
12. Costes S, Streuli CH, Barcellos-Hoff MH (2000) Quantitative image analysis of laminin immunoreactivity in skin basement membrane irradiated with 1 GeV/nucleon iron particles. *Radiat Res* 154:389–397.
13. Magee JL, Chatterjee A (1980) Radiation chemistry of heavy-particle tracks. 1. General considerations. *J Phys Chem* 84:3529–3536.
14. Chatterjee A, Maccabee HD, Tobias CA (1973) Radial cutoff LET and radial cutoff dose calculations for heavy charged particles in water. *Radiat Res* 54:479–494.
15. Tobias CA, et al. (1971) Radiological physics characteristics of the extracted heavy ion beams of the bevatron. *Science* 174:1131–1134.
16. Jakob B, Splinter J, Taucher-Scholz G (2009) Positional stability of damaged chromatin domains along radiation tracks in mammalian cells. *Radiat Res* 171:405–418.
17. Sachs RK, Chen AM, Brenner DJ (1997) Review: Proximity effects in the production of chromosome aberrations by ionizing radiation. *Int J Radiat Biol* 71:1–19.
18. Sachs RK, Ponomarev AL, Hahnfeldt P, Hlatky LR (1999) Locations of radiation-produced DNA double strand breaks along chromosomes: A stochastic cluster process formalism. *Math Biosci* 159:165–187.
19. Aten JA, et al. (2004) Dynamics of DNA double-strand breaks revealed by clustering of damaged chromosome domains. *Science* 303:92–95.
20. Jakob B, Splinter J, Durante M, Taucher-Scholz G (2009) Live cell microscopy analysis of radiation-induced DNA double-strand break motion. *Proc Natl Acad Sci USA* 106:3172–3177.
21. Lisby M, Mortensen UH, Rothstein R (2003) Colocalization of multiple DNA double-strand breaks at a single Rad52 repair centre. *Nat Cell Biol* 5:572–577.
22. Savage JR (1996) Insight into sites. *Mutat Res* 366:81–95.
23. Savage JR (2002) Reflections and meditations upon complex chromosomal exchanges. *Mutat Res* 512:93–109.
24. Anderson RM, Stevens DL, Goodhead DT (2002) M-FISH analysis shows that complex chromosome aberrations induced by alpha -particle tracks are cumulative products of localized rearrangements. *Proc Natl Acad Sci USA* 99:12167–12172.
25. Anderson RM, et al. (2007) Effect of linear energy transfer (LET) on the complexity of alpha-particle-induced chromosome aberrations in human CD34+ cells. *Radiat Res* 167:541–550.
26. Du G, et al. (2011) Spatial dynamics of DNA damage response protein foci along the ion trajectory of high-LET particles. *Radiat Res*, in press.
27. Ponomarev AL, Costes SV, Cucinotta FA (2008) Stochastic properties of radiation-induced DSB: DSB distributions in large scale chromatin loops, the HPRT gene and within the visible volumes of DNA repair foci. *Int J Radiat Biol* 84:916–929.
28. Hauptner A, et al. (2006) DNA-repair protein distribution along the tracks of energetic ions. *Radiat Prot Dosimetry* 122:147–149.
29. Nikjoo H, O'Neill P, Goodhead DT, Terrissol M (1997) Computational modelling of low-energy electron-induced DNA damage by early physical and chemical events. *Int J Radiat Biol* 71:467–483.
30. Nikjoo H, O'Neill P, Wilson WE, Goodhead DT (2001) Computational approach for determining the spectrum of DNA damage induced by ionizing radiation. *Radiat Res* 156:577–583.
31. Wang H, et al. (2001) Efficient rejoining of radiation-induced DNA double-strand breaks in vertebrate cells deficient in genes of the RAD52 epistasis group. *Oncogene* 20:2212–2224.
32. Karlsson KH, Radulescu I, Rydberg B, Stenerlow B (2008) Repair of radiation-induced heat-labile sites is independent of DNA-PKcs, XRCC1 and PARP. *Radiat Res* 169:506–512.
33. Kato TA, Okayasu R, Bedford JS (2008) Comparison of the induction and disappearance of DNA double strand breaks and gamma-H2AX foci after irradiation of chromosomes in G1-phase or in condensed metaphase cells. *Mutat Res* 639:108–112.
34. Leatherbarrow EL, Harper JV, Cucinotta FA, O'Neill P (2006) Induction and quantification of gamma-H2AX foci following low and high LET-irradiation. *Int J Radiat Biol* 82:111–118.
35. Chiolo I, et al. (2011) Double-strand breaks in heterochromatin move outside of a dynamic HP1a domain to complete recombinational repair. *Cell* 144:732–744.
36. Jakob B, et al. (2011) DNA double-strand breaks in heterochromatin elicit fast repair protein recruitment, histone H2AX phosphorylation and relocation to euchromatin. *Nucleic Acids Res* 39:6489–6499.
37. Bakkenist CJ, Kastan MB (2003) DNA damage activates ATM through intermolecular autophosphorylation and dimer dissociation. *Nature* 421:499–506.
38. Baure J, et al. (2009) Histone H2AX phosphorylation in response to changes in chromatin structure induced by altered osmolarity. *Mutagenesis* 24:161–167.
39. Costes S, et al. (2001) Large-mutation spectra induced at hemizygous loci by low-LET radiation: Evidence for intrachromosomal proximity effects. *Radiat Res* 156:545–557.
40. Brenner DJ, Sachs RK (2006) Estimating radiation-induced cancer risks at very low doses: Rationale for using a linear no-threshold approach. *Radiat Environ Biophys* 44:253–256.
41. Hickson I, et al. (2004) Identification and characterization of a novel and specific inhibitor of the ataxia-telangiectasia mutated kinase ATM. *Cancer Res* 64:9152–9159.
42. Bocker W, Iliakis G (2006) Computational Methods for analysis of foci: Validation for radiation-induced gamma-H2AX foci in human cells. *Radiat Res* 165:113–124.
43. Olivo-Marin JC (2002) Extraction of spots in biological images using multiscale products. *Pattern Recognition* 35:1989–1996.